J Nanopart Res (2020) 22: 217
https://doi.org/10.1007/s11051-020-04926-3

RESEARCH PAPER

Morphology-dependent of nanosizes CdS toward efficient photocatalytic Cr (VI) reduction

Ying Cao · Hongfei Yin · Tianle Fan · Xiaoheng Liu · Shenming Chen

Received: 7 January 2020 / Accepted: 16 June 2020 / Published online: 21 July 2020

Abstract CdS with different morphologies were prepared by simple methods (mainly by water bath) with different solvents, including CdS nanoparticles (CdS-0), CdS nanorods (CdS-1), CdS nanosheets (CdS-2), and CdS nanospheres (CdS-3). The structures and morphologies of as-prepared samples were characterized by XRD, XPS, UV–vis DRS, TEM, and SEM. All the prepared samples were used for the photoreduction of Cr (VI) to characterize the photocatalytic performance. CdS-1 shows the highest photocatalytic efficiency was prepared by simply stirring using ethylenediamine as solvent and thiourea as the sulfur source; 98.4% of Cr (VI) can be reduced to Cr (III) within 25 min. The increased photocatalytic activity can be attributed to the high crystallinity and purity, fast separate efficiency, and migration efficiency of electrons (e^-) and holes (h^+), as well. This work showed that morphologies and crystallinities have significant impact on the Cr (VI) photoreduction efficiency and introduced a simple method for fabricating samples with different morphologies, which add the knowledge for Cr (VI) reduction. Hoping our work can provide a tendency to fabricate efficient photocatalysis via a simple method.

Keywords CdS · Cr (VI) photoreduction · Morphology · Nanomaterials · Nanostructured catalysts

Electronic supplementary material The online version of this article (https://doi.org/10.1007/s11051-020-04926-3) contains supplementary material, which is available to authorized users.

Y. Cao · H. Yin · T. Fan · X. Liu (✉)
Key Laboratory for Soft Chemistry and Functional Materials of Ministry of Education, School of Chemical Engineering, Nanjing University of Science and Technology, Nanjing 210094, China
e-mail: xhliu@njust.edu.cn

S. Chen (✉)
Department of Chemical Engineering and Biotechnology, National Taipei University of Technology, Taipei 106, Taiwan
e-mail: smchen78@ms15.hinet.net

Introduction

Energy and the environment are two major problems facing the world today. Since the discovery of TiO_2 used as the catalyst for water splitting under light irradiation (Fujishima et al. 2018; Fujishima and Honda 1972), semiconductor photocatalytic technology was recognized as promising ways to meet the requirements of these two problems. However, due to the unsatisfactory bandgap of pure TiO_2, only UV and an extremely small part of visible light could be utilized for photocatalysis, which has a great limitation on the conversion efficiency of solar light, making photocatalysis technology difficult to be applied on a large scale. Therefore, semiconductor photocatalysts with visible even near-infrared light response have been extensively investigated for water splitting (Wang et al. 2019; Ai et al. 2019), reduction of CO_2 to high-value chemical products (Kar et al. 2019; Maimaitizi et al. 2020), reduction of dinitrogen to ammonia (Lv et al. 2019; Sun et al. 2019a), and environmental remediation (Yu et al. 2019; Ruby et al. 2020; Bai et al. 2020).

Cr (VI) is one of the most toxic inorganic contaminants detected in water sources and has been recognized

to be a carcinogenic and mutagenic substance. Treating wastewater containing Cr (VI) in a cost-effective route has aroused strong enthusiasm from both academia and industry (Chen et al. 2020; Yu et al. 2020; Zeng et al. 2019). In general, converting Cr (VI) into Cr (III) is a common route for dealing with Cr (VI) aqueous solution, because Cr (III) is non-toxic and is an indispensable trace element in the human body. In addition, Cr (III) could be precipitated in the form of Cr $(OH)_3$ and eliminated as solid waste. In recent years, reduction of Cr (VI) over semiconductor photocatalysts have been widely used to deal with Cr (VI) aqueous solutions due to their advantages of simple operation, carried out under ambient conditions, low cost, high efficiency, and direct utilization of sunlight (Chen et al. 2019; Khan et al. 2020; Peng et al. 2019).

It could be concluded from previous reports that morphology, crystal structure, crystallinity, and particle size are all factors that have influences on the photocatalytic performances on CdS (Khan et al. 2018; Mu et al. 2020). The bandgap structure, separation, and transport of charge carriers and reaction at the interface of photocatalyst/electrolyte are all related to the above-mentioned factors. Until now, a great deal of methods have been developed to synthesize CdS nanocrystals with distinct morphologies, such as nanorods (Mu et al. 2020; Liu et al.2019; Kumar et al.2017; Ma et al. 2017a), nanosheets (Ma et al. 2017a; Qiu et al. 2019; Sun et al. 2019b), nanotube (Sun et al. 2019b; Li et al. 2012), micro/nano leaves (Li et al. 2012; Bie et al. 2019), hollow structures (Bie et al. 2019; Shen et al. 2010; Jing and Guo 2006), nanosteps (Jing and Guo 2006; Muruganandham et al. 2009), and microtowers (Muruganandham et al. 2009; Yu et al. 2014). Yu et al. (2014), Bie et al. (2018) reported a morphology-controlled CdS photocatalysts by changing the sulfur source and solvent for photocatalytic H_2 evolution. Bie et al. (2018), Liu et al. (2018a) reported a thickness tunable CdS nanosheets by adjusting the amount of sodium citrate for efficient hydrogen production. Liu et al. (2018a), Qu et al. (2013) reported a mixed-solvothermal route to fabricate CdS with different morphologies for hydrogen evolution. However, all of them were focused on the photocatalytic hydrogen evolution; to the best of our knowledge, there were few reports on the reduction of Cr (VI) over CdS with different morphologies.

Herein, a series of CdS with different morphologies were fabricated through a simple method. We report the chemical bath method to synthesis the samples. As far as we know, morphologies have an unignorable effect on the performance, the photocatalytic Cr (VI) reduction experiments are carried out under ambient, and neutral conditions were employed to evaluate the photocatalytic performances of the CdS with different morphologies. Systematically, characterizations were employed to investigate the influence of different morphologies; the factor of the enhanced photocatalytic performance also investigated.

Experimental

Sample preparation

Preparation of CdS nanoparticles (denoted as CdS-0)

About 1 mmol $Cd(Ac)_2{\cdot}2H_2O$ and 2 mmol thiourea were added into 100 mL deionized water in sequence under continuous magnetic stirring at room temperature; next, the mixture was heated to 65 °C, the pH of the mixture was adjusted to 10.5 by using NaOH aqueous solution, then the reaction system was kept for 90 min. Finally, the generated orange sample was collected by centrifugation, washing, and dried at 60 °C for 12 h.

Preparation of CdS nanorods (denoted as CdS-1)

About 10 mmol $Cd(NO)_3{\cdot}4H_2O$ and 30 mmol thiourea were dissolved in 60 mL ethylenediamine under room temperature; after stirred for 60 min, the mixture was transferred into 100 mL autoclave and maintained at 180 °C for 24 h. After cooled to room temperature naturally, the resulted sample was collected and washed with water and absolute ethanol, then dried at 60 °C overnight.

Preparation of CdS nanosheets (denoted as CdS-2)

About 5 mmol sodium citrate was dissolved in 50 mL of deionized water; then, 10 mL aqueous solution containing 3 mmol $CdCl_2{\cdot}2.5H_2O$ was added after stirred for 20 min at room temperature; 5 mL 28 wt% $NH_3{\cdot}H_2O$ and 10 mL aqueous solution containing 9 mmol thiourea were dropwise added in sequence; after stirred for 20 min, the reaction system was transferred and heated in the water bath at 60 °C for 3 h under continuous stirring. After cooled to room temperature, the light-yellow product was centrifuged and washed by DI water and absolute ethanol for three times, respectively; then, the sample was dried at 60 °C overnight.

Preparation of CdS nanospheres (denoted as CdS-3)

About 24 mL 0.1 M sodium citrate aqueous solution and 40 mL 0.05 M $CdCl_2 \cdot 2.5H_2O$ aqueous solution were added into 100 mL deionized water; after stirred for 20 min at room temperature, 5.6 mL 28 wt% $NH_3 \cdot H_2O$ and 10 mL 1.2 M thiourea aqueous solutions were dropwise added in sequence; then, the reaction system was transferred and heated in water bath at 60 °C for 3 h under continuous stirring. After cooled to room temperature, the light-yellow product was centrifuged, then washed with DI water and ethanol for at least 3 times, respectively, then dried at 60 °C overnight.

Characterization

The structures of the as-prepared crystals were characterized through the instrument of Bruker D8 Advance powder X-ray diffractometer radiated by Cu Kα (λ = 0.15418 nm). The morphologies, as well as microstructures of the obtained samples, were characterized by field-emission scanning electron microscope (FESEM, Hitachi S-4800) and transmission electron microscope (TEM, JEOL JEM-2100). Evolution 220 UV–vis spectrophotometer was carried out to characterize UV–vis diffused reflectance spectra (Thermo Fisher, America) and the wavelength was between 200 and 800 nm. The composition of the as-prepared samples was characterized by X-ray photoelectron spectroscopy (XPS) with an XSAM800 apparatus. Photoelectron spectrometer was carried out on PHI Quantera II SXM to analyze the surface element and electronic binding energy under an Al Kα radiation (λ = 0.84 nm). FL3-TCSPC fluorescence spectrophotometer was employed to reflect the solid phase (λ_{ex} = 325 nm) and liquid phase (λ_{ex} = 320 nm) photoluminescence spectrum.

Electrochemical analysis

Electrochemical performances were analyzed via electrochemical impedance spectroscopy (EIS), Mott–Schottky curve (MS), and photocurrent measurements. All the above were carried out on a normal three-electrode electrochemical workstation. Ag/AgCl electrode was employed as reference electrode, and Pt wire electrode was employed as counter electrode. For EIS measurements, the curves were recorded from 100 kHz to 0.01 Hz in a mixed solution containing 0.5 M KCl aqueous solution and 5.0 mM $K_3[Fe(CN)_6]$/$K_4[Fe(CN)_6]$. Na_2SO_4 aqueous solution, with a concentration of 0.5 M, was used as the electrolyte to measure Mott–Schottky and photocurrent performances. The light source was a 300 W Xe lamp. The working electrode in this work was prepared as below: 4 mg CdS with different morphologies were added into a mixed solvent containing 750 μL water and 250 μL ethanol solution; then, adding 10 μL Nafion solution (5 wt%), the mixtures were ultrasonically for 1 h to produce a homogeneous slurry. Finally, the dispersions with a volume of 150 μL were dropped onto an ITO-coated glass substrate, the area of the glass is 1 cm × 3 cm, and the coating area was about 1 cm^2.

Photocatalytic tests

The photocatalytic performances of the as-obtained samples were performed by the reaction of Cr (VI) reduction under simulated visible light irradiation. The light was originated from a 300-W Xe lamp equipped with a 400-nm filter. The photocatalytic process was carried out as follows: 30 mg sample was added to 50 mL solution containing 20 mg/L Cr (VI); then, the above suspensions were vigorously stirred in dark for 1 h before illumination to achieve the adsorption-desorption equilibrium. About 3 mL of the reaction suspensions were taken out at certain time intervals; after removing the photocatalyst through centrifugation, the filtrate was measured via UV–vis spectrometer (the model number is UV-1801) to know the concentration of Cr (VI). The ultimate concentration of Cr (VI) was analyzed colorimetrically at the wavelength of 540 nm (Zhu et al. 2017).

Results and discussions

XRD and XPS analysis

The crystal structure of the as-obtained photocatalysts was characterized by powder X-ray diffractometer, as illustrated in Fig. 1a. It could be obviously observed that all the peaks are consistent with JCPDS 41-1049, without any impurity crystal phase, indicating the as-fabricated samples possess the crystal phase of hexagonal structure and the high purity of the as-prepared samples. On the other hand, the as-prepared CdS-1 exhibited the highest crystallinity, followed by CdS-0, CdS-2, and CdS-3 displayed poor crystallinity. In general, the higher the crystallinity, the less the lattice defects, which is more

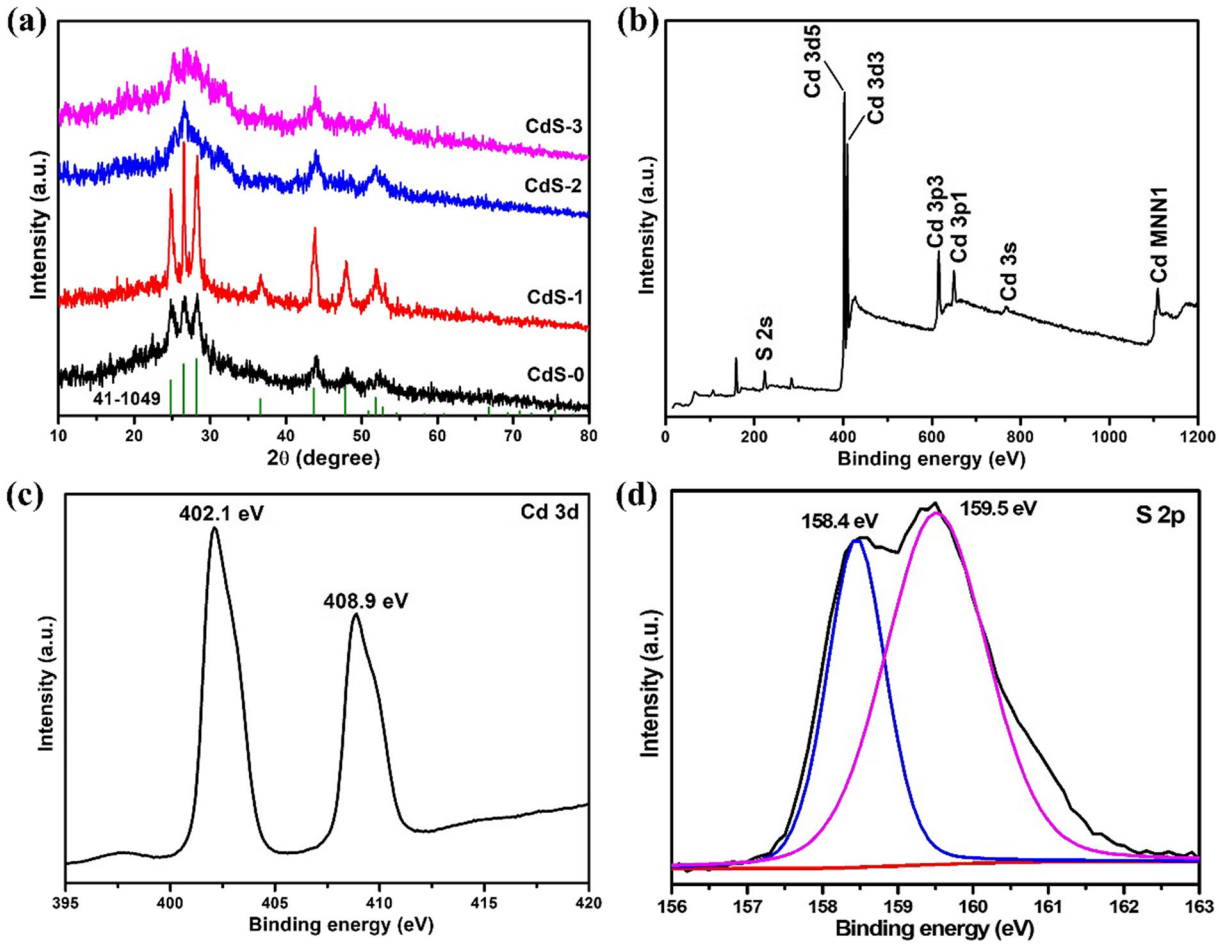

Fig. 1 **a** XRD patterns of the as-prepared samples, XPS of CdS-1: **b** full spectrum, **c** Cd 3d, and **d** S 2p

conducive to the transport of the charge carriers. Furthermore, the surface chemical state of each element in the as-fabricated CdS-1 was measured by XPS, shown in Fig. 1b–d. It could be apparently observed that Cd and S elements were included in the as-prepared sample from the full spectrum of the sample (Fig. 1b), confirming the formation of CdS. Two characteristic signals located at 402.1 and 408.9 eV (Fig. 1c) for Cd 3d could be assigned to Cd $3d_{7/2}$ and Cd $3d_{5/2}$, implying the chemical state of Cd element in the CdS-1 exists mainly in the form of Cd^{2+}. As for S element, the characteristic peaks at 158.1 and 159.4 eV (Fig. 1d) could be indexed into S $2p_{3/2}$ and S $2p_{1/2}$.

Morphology analysis

Different morphologies of CdS were prepared through a simple chemical bath method and hydrothermal method with different solvents. The morphologies of as-prepared samples were investigated by SEM (Fig. 2a–j) and TEM (Fig. 2b–k) below. Figure 2a and b shows CdS-0 with small size (about 10 nm); all the nanoparticles were aggregated together. Figure 2d and f displays lots of small CdS nanorods (CdS-1), and there are not any other morphologies. CdS nanosheets (CdS-2) were shown in Fig. 2g, h with many thin layers. Besides few pieces of nanosheets, there are many uniform CdS nanospheres (CdS-3) displayed in Fig. 2j, k with the diameter of about 100 nm. In corresponding to the XRD patterns of CdS-3, the sizes of CdS-3 are the smallest, so we can conclude that the nanospheres are secondary particles clustering by primary particles. The corresponding HRTEM of the as-prepared samples was shown in Fig. 2c, f, i, and l. The lattice spacing of 0.336 nm corresponding to (002) plane of CdS (highlight in red color, the same below) in Fig. 2c, f, and i

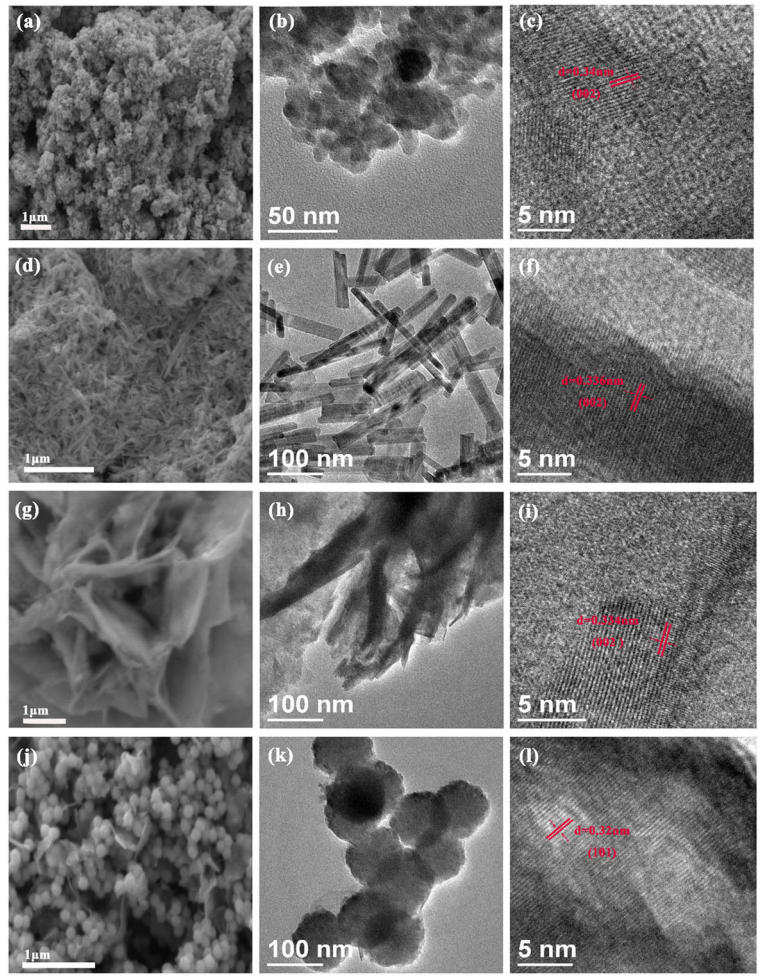

Fig. 2 **a, d, g**, and **j** SEM images of as-prepared samples with different morphologies; **b, e, h,** and **k** TEM image of as-prepared CdS-0, CdS-1, CdS-2, CdS-3; **c, f, i,** and **l** HRTEM image of CdS-0, CdS-1, CdS-2, and CdS-3

represents hexagonal phase (Ma et al. 2017b; Jia et al. 2018), while the lattice spacing of 0.32 nm corresponding to (101) plane in Fig. 2l. From the HRTEM we can conclude that the enhanced photocatalytic performance has little contact with the exposed crystal plane.

Optical properties

The UV–vis DRS spectra were investigated to analyze the optical properties of the as-obtained photocatalysts as displayed in Fig. 3a. It could be easily observed that all the as-obtained photocatalysts exhibited strong visible light absorption, where CdS-0 showed the strongest visible light absorption, followed by CdS-1 and CdS-2; the CdS-3 displayed the weakest absorption among all the as-prepared samples. In general, the higher the light absorption, the better the photocatalytic performances of the photocatalyst.

The bandgap of the as-fabricated four samples was further calculated via the following equation: $\alpha h\nu = A(h\nu\text{-}E_g)^{n/2}$, in which α is absorption index, h is the Planck's constant, ν is the frequency of vibration, A is a proportional constant value, and E_g is bandgap energy of the semiconductor (Yi et al. 2019; Zhang et al. 2019). According to the previous report that CdS is an indirect transition type semiconductor, therefore, the value of n for calculation, the bandgap of CdS is 4. The corresponding bandgap of CdS-0, CdS-1, CdS-2, and CdS-3 was 2.11 eV, 2.26 eV, 2.26 eV, and 2.30 eV, respectively.

BET

The N_2 adsorption-desorption isotherms and corresponding pore size distribution graphs were carried out to test the specific surface area of CdS with different

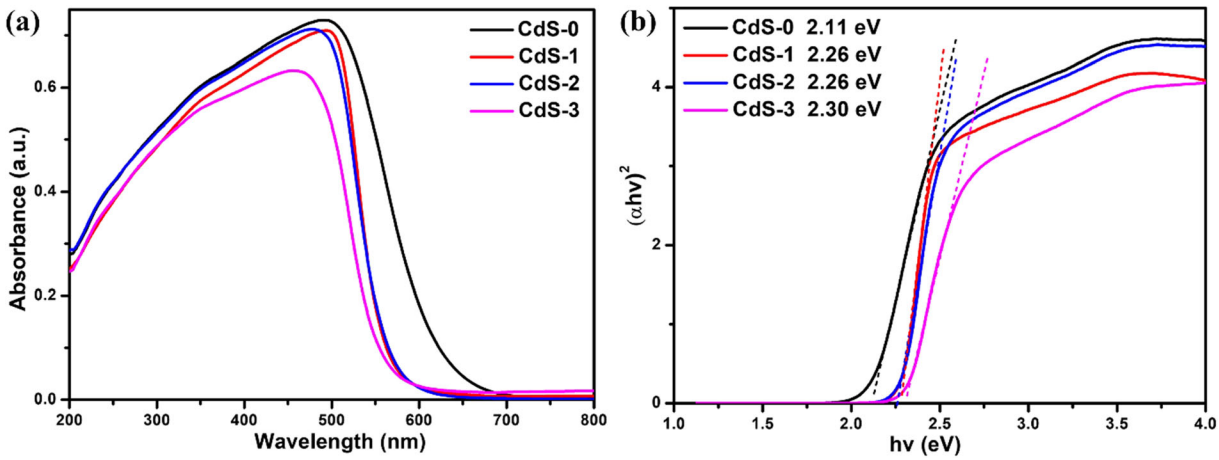

Fig. 3 **a** UV–vis diffused reflectance spectra of the as-fabricated samples; **b** the Kubelka-Munk transformed function of the as-prepared samples

morphologies, as shown in Fig. 4. All the samples exhibit the type IV isotherms, suggesting the existence of mesoporous structure; the corresponding pore-size distribution was estimated by BJH method according to the desorption branch of the isotherm; the inset graph in Fig. 4b shows that the pore structures of the as-prepared CdS-1 are all mesoporous structure, while other morphologies of CdS contain both mesoscale and macroscale pores. According to the report, the specific surface areas of CdS-0, CdS-1, CdS-2, and CdS-3 are 71.9747 m^2/g, 25.6765 m^2/g, 17.1323 m^2/g, and 37.7781 m^2/g, respectively. The specific surface area of the optimistic sample is not the maximum; this indicates that the photocatalytic efficiency is not controlled by specific surface area here.

Photocatalytic performance

Photocatalytic reduction of Cr (VI) under visible light irradiation was carried out to evaluate the photocatalytic activities of the as-fabricated photocatalysts. The UV −visible spectral changes of Cr (VI) photo reduced by CdS-1 at certain illumination time under simulated visible light is shown in Fig. 5a. After the photo reduction process was undergone for 25 min, a negligible characteristic peak at 540 nm could be observed, indicating the high efficiency of the photocatalytic performance of CdS-1 for Cr (VI) photo reduction. Figures 5b and 4c display typical photocatalytic reduction efficiency curves and reaction kinetic curves of Cr (VI) over different samples under visible light irradiation. The removal efficiencies of Cr (VI) over CdS-0, CdS-2, and CdS-3 were 98.9%, 25.0%, and 75.8% within 40 min, respectively. However, the removal efficiency of CdS-1 reached 98.4% within 25 min irradiation. The reaction kinetic curves of Cr (VI) photocatalytic reduction under visible light irradiation were fitted by quasi first-order method, the kinetic constant was figured out by the equation of $\ln(C_0/C_t) = kt$, C_0 is the concentration of Cr (VI) after the whole system reaching the adsorption–desorption equilibration, C_t is the concentration of Cr (VI) at certain illumination interval, and the k in the equation above is the kinetic constant. The corresponding k of CdS-0, CdS-1, CdS-2, and CdS-3 were 0.11389 min^{-1}, 0.15599 min^{-1}, 0.00742 min^{-1}, and 0.03635 min^{-1}, respectively. The CdS-1 exhibited the highest photocatalytic performances, which is nearly 21 times higher than that of CdS-2. Figure 5d shows that CdS-1 exhibited the best photocatalytic efficiency under the same pH; Fig. 5e shows the optimum pH of CdS-1 for photocatalytic reaction; Cr(VI) can be photo reduced thoroughly in 5 min by CdS-1 when the pH value is 2.

Stability and recyclability

Stability is an important characteristic of the as-prepared photocatalyst; to explore the stability of the best sample, recycle experiments were carried out for five times. When the photocatalytic reaction is finished, recycling the sample by ultrasonics and then washing with DI water and pure ethanol for at least three times, then the sample was dried at 60 °C for 12 h. A conclusion can be reached from Fig. 6a that in the fifth recycle, CdS-1 remains relatively high photocatalytic performance,

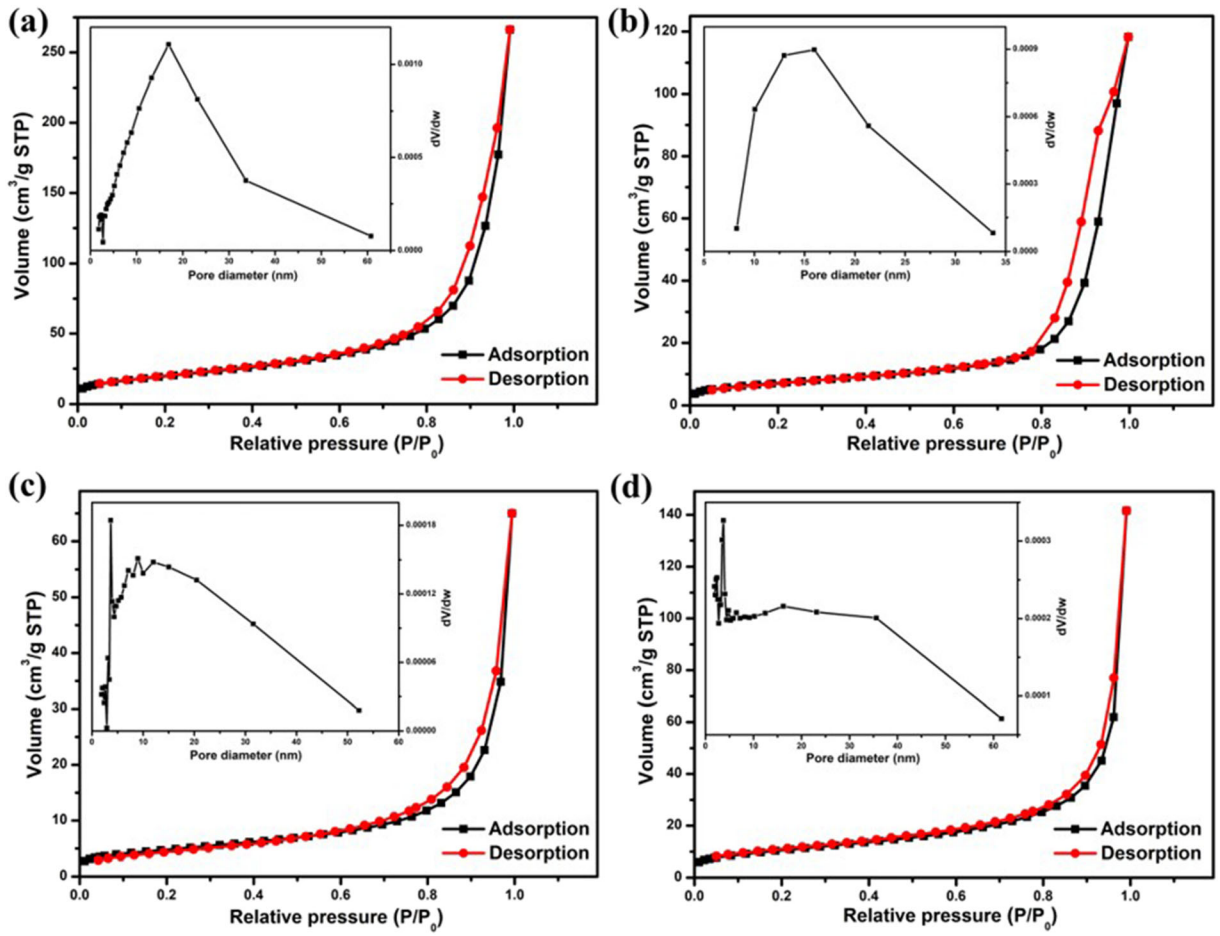

Fig. 4 Nitrogen adsorption-desorption isotherms and the corresponding pore-size distribution curves (inset) of CdS-0 (**a**), CdS-1 (**b**), CdS-2 (**c**), and CdS-3 (**d**)

which indicates that the catalyst has high stability during the photocatalytic reactions. Figure 6b indicates that CdS-1 after shows the similar peaks as CdS-1 fresh; Fig. 6c suggests that the morphology of as-prepared CdS-1 did not change after the reaction. These facts confirm that the as-prepared CdS-1 has good stability. Figure 6d exhibits the XPS spectra of Cr species after the photocatalytic reaction. According to the previous articles (Li et al. 2015), the characteristic binding energy peaks at 577.0–580.0 eV and 586.0–588.0 eV are belonging to Cr (III), while 580.0–580.5 eV and 589.0–590.0 eV are belonging to Cr(VI). As shown in Fig. 5d, the binding energies of 578.38 and 587.78 eV assigned to Cr (III). The result suggests that Cr(VI) can be reduced to Cr(III) after the photocatalytic reaction.

The curves of transient photocurrent versus time (i-t curve) of the CdS with different morphologies were measured to investigate the efficiency of charge separation within the as-prepared samples. Figure 7a exhibits the current-time curve over different electrodes with several switching cycles under periodic irradiation in a 0.5 M Na_2SO_4 aqueous solution. Generally, the stronger photocurrent density of the photoelectrode always possesses the higher separation efficiency of photoexcited charge carriers (Gopannagari et al. 2017). It could be obviously observed that the photoelectrode of CdS-1 displayed the strongest photocurrent density among these four photoelectrodes, indicating that the photoinduced charge carriers generated in CdS-1 had the highest separation efficiency. The electrochemical impedance spectrum (EIS) of the as-fabricated photoelectrodes was displayed in Fig. 7b, which was applied to evaluate the transfer efficiency of the charge carriers. In general, the diameters of the semicircle in

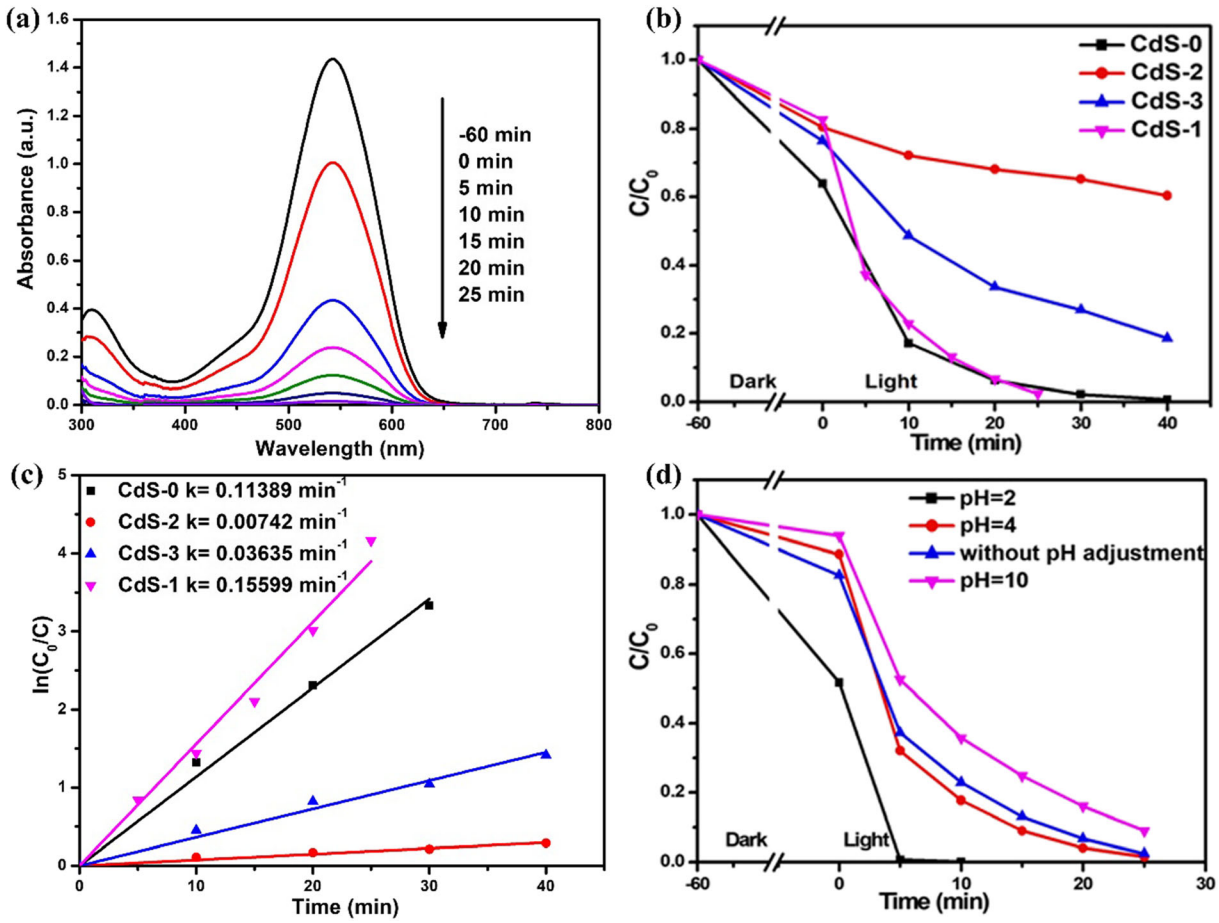

Fig. 5 **a** UV–vis absorption spectra for reduction of Cr (VI) over CdS-1; **b** photocatalytic performances of Cr (VI) reduction over different samples; **c** the rate constants of the as-prepared photocatalysts for the reduction of Cr (VI); **d** photocatalytic performance of CdS-1 under different pH

EIS reflect the charge transfer resistance, the smaller radius of the semicircle, and the lower the charge transfer resistance at the electrode–electrolyte interface (Ma et al. 2017b; Ri et al. 2018; Zhu et al. 2018). Compared with the other three samples, it could be obviously observed that the as-prepared CdS-1 exhibited the smallest radius of the semicircle, which indicates that the CdS-1 had an efficient charge transfer than other samples at the electrode-electrolyte interface.

To fully understand the mechanism of the photocatalytic reaction, Mott–Schottky measurement and UV–vis DRS were carried out simultaneously to calculate the accurate E_g and CB of the as-prepared four samples. Figure 8 exhibits the Mott–Schottky curve of CdS-0, CdS-1, CdS-2, and CdS-3. It can be observed that all the four curves exhibit positive slop of $1/C^2$-potential curves indicating that the as-fabricated CdS samples were characterized as n-type semiconductors. Figure 8 shows that the flat band potentials of CdS-0, CdS-1, CdS-2, and CdS-3 were −0.66 V, −0.75 V, −0.64 V, and − 0.63 V (vs. Ag/AgCl), respectively. When the reference electrode is Ag/AgCl electrode, the difference between the conduction band and flat band is 0.197 V, so the conduction band of CdS-0, CdS-1, CdS-2, and CdS-3 can be figured as −0.463 eV, −0.553 eV, −0.443 eV, and − 0.433 eV (vs. NHE) (Liang et al. 2015), respectively. Combine the UV–vis DRS curve and Mott–Schottky curve in assistant with the equation of $E_{VB} = E_{CB}$-E_g, the corresponding valence band positions were 1.647 eV, 1.707 eV, 1.817 eV, and 1.867 eV (vs. NHE), respectively.

In order to investigate the active species generated in the photocatalytic Cr (VI) reduction process, a series of active species trapping experiments were carried out, as depicted in Fig. 9a. Isopropyl alcohol (IPA), silver nitrate

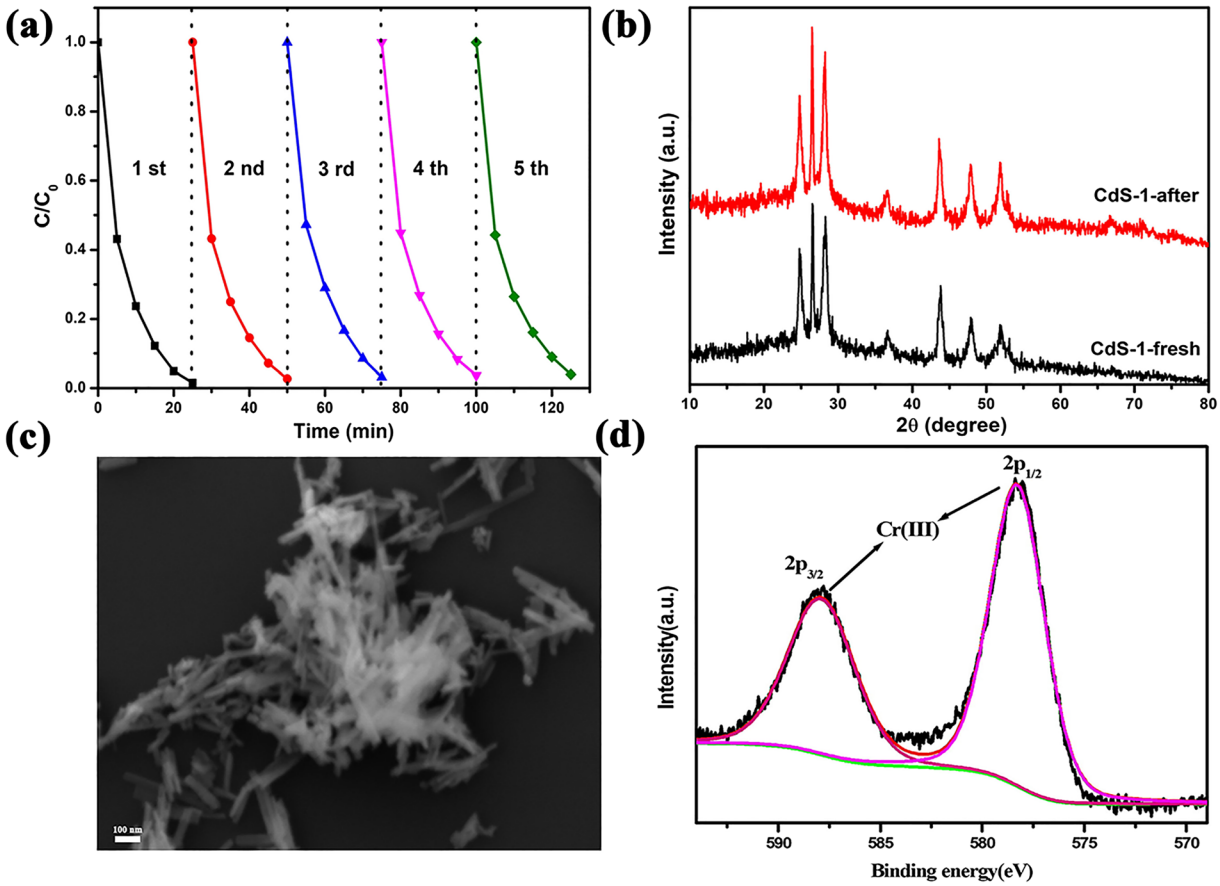

Fig. 6 **a** Recycle experiments of CdS for the reduction of Cr (VI); **b** XRD patterns of samples before and after the photoreduction reactions; **c** FE-SEM of CdS-1 after reaction, the scale bar in the image is 100 nm; **d** XPS spectra of Cr 2p after the photocatalytic reaction

($AgNO_3$), and disodium ethylenediaminetetraacetate (EDTA-2Na) with a concentration of 1 mM were scavengers in the trapping experiment to capture·OH, e^-, and h^+, respectively. In addition, nitrogen was introduced to get rid of the formation of $\cdot O_2^-$ generated from the reaction between dissolved oxygen and photogenerated

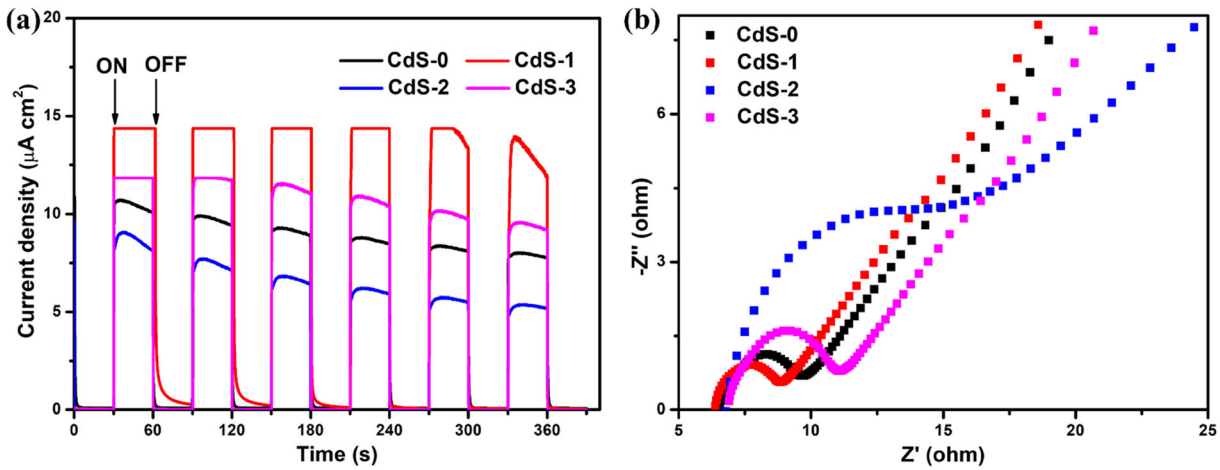

Fig. 7 **a** Transient photocurrent responses of all samples and **b** electrochemical impedance spectra of the as-fabricated photocatalysts

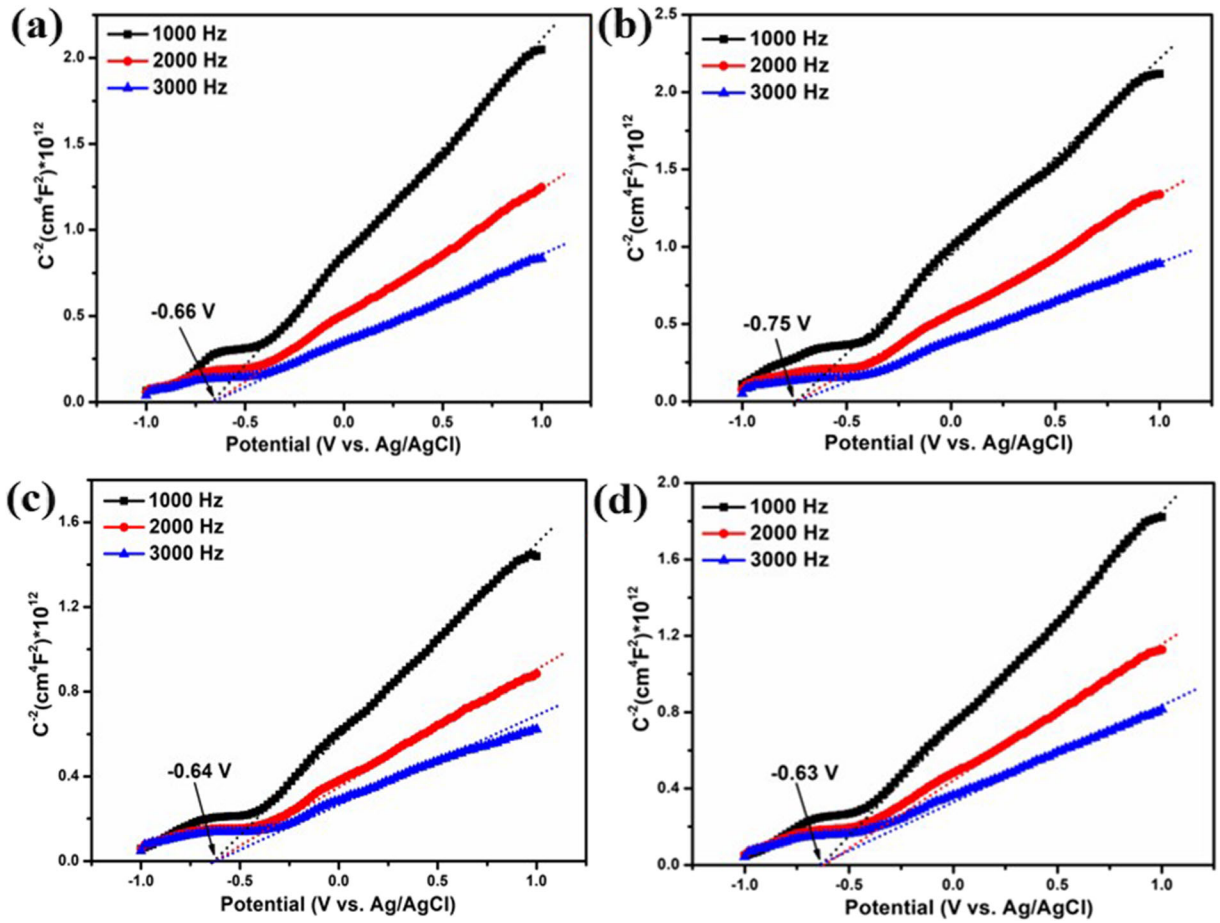

Fig. 8 Mott–Schottky plots of CdS-0 (**a**), CdS-1 (**b**), CdS-2 (**c**), and CdS-3 (**d**) in 0.5 M Na_2SO_4 aqueous solution

electrons. It could be easily observed that the reduction efficiency of Cr (VI) decreased significantly after the addition of $AgNO_3$, indicating that the Cr (VI) was reduced to Cr (III) by photoexcited electrons on the surface of CdS step by step via one-electron reaction route (Eq. (1)) (Li et al. 2012; Wang et al. 2016). It was

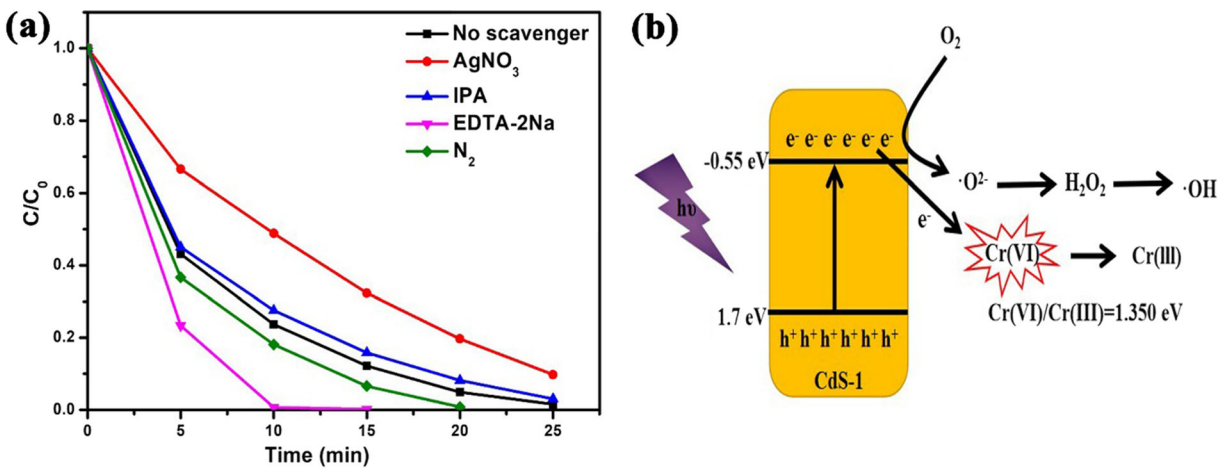

Fig. 9 **a** Effects of different scavengers on Cr (VI) reduction in the presence of CdS-1; **b** schematic diagram

Table 1 Scavengers and the process it can suppress or facilitate

Addictive	Mechanism Analysis
$AgNO_3$	$Cr(VI) \rightarrow^{e^-} Cr(V) \rightarrow^{e^-} CR(IV) \rightarrow^{e^-} Cr(III)$ (1)
N_2	$O_2 + e^- \rightarrow \cdot O_2^-$ (2)
IPA	$\cdot O_2^- + 2H^+ + e^- \rightarrow H_2O_2$ (3)
	$H_2O_2 + e^- \rightarrow \cdot O_2^- + OH^-$ (4)
EDTA-2Na	h^+ scavenger

reported that the existence of oxygen might compete with Cr (VI) species for the photoexcited electrons (Liu et al. 2018b; Yang et al. 2016), when N_2 was continuously bubbled into the photocatalytic reaction system, the oxygen was removed from the aqueous, inhibiting the generation of $\cdot O_2^-$, as listed Eq. (2), resulting in the improvement of the Cr (VI) reduction efficiency. As the IPA was introduced into the photoreduction process, the reduction efficiency had a slight decrease, indicating that when the ·OH was trapped by IPA, the photoreduction efficiency of Cr (VI) is lower than before; the reason for the decreased reduction efficiency could be ascribed to that when the ·OH trapped by IPA; the concentration of ·OH becomes very low, so the reaction equilibrium shifts toward ·OH generation as listed in Eqs. (2)–(4) (Li et al. 2012; Ma et al. 2017b; Isaka et al. 2018); therefore, there might be a competitive relationship between the generation of ·OH and the reduction of Cr (VI). When the EDTA-2Na was added into the photoreduction process as h^+ scavenger, the reduction efficiency of Cr (VI) had an obvious increase; the reason for the improvement of the Cr (VI) reduction efficiency could be assigned to that the photogenerated holes were trapped, boosting the separation efficiency of photoinduced electrons and holes, leading to the enhancement of the photocatalytic reduction efficiency. Therefore, the main active species for the photocatalytic reduction of Cr (VI) was photogenerated electrons. Scavengers and the process it can suppress or facilitate were shown in Table 1. Figure 9b shows the schematic diagram of CdS in accordance with the trapping experiments.

Conclusions

In this work, we mainly synthesize CdS with different morphologies by the easy method with different solvent. Cr (VI) photoreduction reaction was carried out in the ambient and neutral condition. We find that solvent has a nonnegligible impact on morphologies and the morphology has an unignorable influence on the photocatalytic performances, especially in this work, the CdS-1 owns the best photocatalytic performance of Cr (VI) reduction and the photoreduction efficiency is 98.4% in 25 min. The result of trapping experiments shows that the active species for Cr (VI) photoreduction is the photo-induced electron and the generation of ·OH waste, a small part of the photo-introduced electron. The enhanced photocatalytic performance can be attributed to the high crystallinity and purity in the corresponding of XRD patterns; besides, in accordance with the transient photocurrent responses and EIS, the structure of CdS nanorods (CdS-1) has an advantage for the fastest separation rate and migrate efficiency of photoinduced electrons (e^-) and holes (h^+); it is also a vital factor for the increased photocatalytic performance.

Funding information This work was supported by the National Natural Science Foundation of China (Grant No. 51872141 and Grant No. 51572126).

Compliance with ethical standards

Conflict of interest The authors declare that they have no conflict of interest.

References

Ai ZZ, Shao YL, Chang B, Zhang L, Shen JX, Wu YZ, Huang BB, Hao XP (2019) Rational modulation of p-n homojunction in P-doped g-C3N4 decorated with Ti_3C_2 for photocatalytic overall water splitting. Appl Catal B-Environ 259

Bai X, Jia J, Du YY, Hu XY, Li JL, Liu EZ, Fan J (2020) Multilevel trapped electrons system in enhancing photocatalytic activity of TiO_2 nanosheets for simultaneous reduction of Cr (VI) and RhB degradation. Appl Surf Sci 503

Bie CB, Fu JW, Cheng B, Zhang LY (2018) Ultrathin CdS nanosheets with tunable thickness and efficient photocatalytic hydrogen generation. Appl Surf Sci 462:606–614

Bie CB, Zhu BC, Xu FY, Zhang LY, Zhang LG (2019) In situ grown monolayer N-doped graphene on CdS hollow spheres with seamless contact for photocatalytic CO_2 reduction. Adv Mater 31(42):1902868

Chen DD, Liu JG, Jia ZZ, Fang JZ, Yang F, Tang YM, Wu K, Liu Z, Fang ZQ (2019) Efficient visible-light-driven hydrogen evolution and Cr(VI) reduction over porous P and Mo co-

doped g-C_3N_4 with feeble N vacancies photocatalyst. J Hazard Mater 361:294–304

Chen FY, Yu CL, Wei LF, Fan QZ, Ma F, Zeng JL, Yi JH, Yang K, Ji HB (2020) Fabrication and characterization of $ZnTiO_3$/$Zn_2Ti_3O_8$/ZnO ternary photocatalyst for synergetic removal of aqueous organic pollutants and Cr((VI)) ions. Sci Total Environ 706:0048–9697

Fujishima A, Honda K (1972) Electrochemical photolysis of water at a semiconductor electrode. Nature 238:37–39

Fujishima M, Ikeda T, Akashi R, Tada H (2018) In situ shape change of Au nanoparticles on TiO_2 by CdS photodeposition: its near-field enhancement effect on photoinduced electron injection from CdS to TiO_2. Acs Omega 3(6):6104–6112

Gopannagari M, Kumar DP, Reddy DA, Hong S, Song MI, Kim TK (2017) In situ preparation of few-layered WS_2 nanosheets and exfoliation into bilayers on CdS nanorods for ultrafast charge carrier migrations toward enhanced photocatalytic hydrogen production. J Catal 351:153–160

Isaka Y, Kondo Y, Kawase Y, Kuwahara Y, Mori K, Yamashita H (2018) Photocatalytic production of hydrogen peroxide through selective two-electron reduction of dioxygen utilizing amine-functionalized MIL-125 deposited with nickel oxide nanoparticles. Chem Commun 54(67):9270–9273

Jia HM, He WW, Zhang BB, Yao L, Yang XK, Zheng Z (2018) Facile synthesis of bismuth oxyhalide nanosheet films with distinct conduction type and photo-induced charge carrier behavior. Appl Surf Sci 441:832–840

Jing DW, Guo LJ (2006) A novel method for the preparation of a highly stable and active CdS photocatalyst with a special surface nanostructure. J Phys Chem B 110(23):11139–11145

Kar P, Zeng S, Zhang Y, Vahidzadeh E, Manuel A, Kisslinger R, Alam KM, Thakur UK, Mahdi N, Kumar P, Shankar K (2019) High rate CO_2 photoreduction using flame annealed TiO_2 nanotubes. Appl Catal B-Environ 243:522–536

Khan AA, Kumari S, Chowdhury A, Hussain S (2018) Phase tuned originated dual properties of cobalt sulfide nanostructures as photocatalyst and adsorbent for removal of dye pollutants. Appl Nano Mater 1(7):3474–3485

Khan AA, Chowdhury A, Kumari S, Hussain S (2020) The facile soft-template-morphology-controlled (STMC) synthesis of ZnIn2S4 nanostructures and their excellent morphology-dependent adsorption properties. J Mater Chem A 8(4): 1986–2000

Kumar DP, Hong S, Reddy DA, Kim TK (2017) Ultrathin MoS_2 layers anchored exfoliated reduced graphene oxide nanosheet hybrid as a highly efficient cocatalyst for CdS nanorods towards enhanced photocatalytic hydrogen production. Appl Catal B-Environ 212:7–14

Li CX, Han LJ, Liu RJ, Li HH, Zhang SJ, Zhang GJ (2012) Controlled synthesis of CdS micro/nano leaves with (0001) facets exposed: enhanced photocatalytic activity toward hydrogen evolution. J Mater Chen 22(45):23815–23820

Li XY, Gao XY, Ai LH, Jiang J (2015) Mechanistic insight into the interaction and adsorption of Cr(VI) with zeolitic imidazolate framework-67 microcrystals from aqueous solution. Chem Eng J 274:238–246

Liang R, Shen L, Jing F, Wu W, Qin N, Lin R, Wu L (2015) NH_2-mediated indium metal–organic framework as a novel visible-light-driven photocatalyst for reduction of the aqueous Cr(VI). Appl Catal B-Environ 162:245–251

Liu Y, Ma YJ, Liu WW, Shang YY, Zhu AQ, Tan PF, Xiong X, Pan J (2018a) Facet and morphology dependent photocatalytic hydrogen evolution with CdS nanoflowers using a novel mixed solvothermal strategy. J Colloid Interf Sci 513:222–230

Liu XN, Du PH, Pan WY, Dang CY, Qian TW, Liu HF, Liu W, Zhao DY (2018b) Immobilization of uranium(VI) by niobate/titanate nanoflakes heterojunction through combined adsorption and solar-light-driven photocatalytic reduction. Appl Catal B-Environ 231:11–22

Liu J, Liang XX, Wang YT, Wang B, Zhang TC (2019) Preparation of CdS nanorods on silicon nanopillars surface by hydrothermal method. Mater Res Bull 120:110591

Lv XS, Wei W, Li FP, Huang BB, Dai Y (2019) Metal-free B@g-CN: visible/infrared light-driven single atom photocatalyst enables spontaneous dinitrogen reduction to ammonia. Nano Lett 19(9):6391–6399

Ma S, Xu XM, Xie J, Li X (2017a) Improved visible-light photocatalytic H_2 generation over CdS nanosheets decorated by NiS_2 and metallic carbon black as dual earth-abundant cocatalysts. Chinese J Catal 38(12):1970–1980

Ma S, Xie J, Wen JQ, He KL, Li X, Liu W, Zhang XC (2017b) Constructing 2D layered hybrid CdS nanosheets/MoS_2 heterojunctions for enhanced visible-light photocatalytic H_2 generation. Appl Surf Sci 391:580–591

Maimaitizi H, Abulizi A, Kadeer K, Talifu D, Tursun Y (2020) In situ synthesis of Pt and N co-doped hollow hierarchical BiOCl microsphere as an efficient photocatalyst for organic pollutant degradation and photocatalytic CO_2 reduction. Appl surf Sci 502

Mu RH, Ao YH, Wu TF, Wang C, Wang PF (2020) Synergistic effect of molybdenum nitride nanoparticles and nitrogen-doped carbon on enhanced photocatalytic hydrogen evolution performance of CdS nanorods. J Alloy Compd 812: 151990

Muruganandham M, Kusumoto Y, Okamoto C, Muruganandham A, Abdulla-Al-Mamun M, Ahmmad B (2009) Mineralizer-assisted shape-controlled synthesis, characterization, and photocatalytic evaluation of CdS microcrystals. J Phys Chem C 113(45):19506–19517

Peng TX, Wen YT, Wang CX, Wang YY, Zhang GS, Zhang YC, Dionysiou DD (2019) Preparation of SnO_2/conjugated polyvinyl alcohol derivative nanohybrid with good performance in visible light-induced photocatalytic reduction of Cr(VI). Mat Sci Semicon Proc 102

Qiu SJ, Shen YL, Wei GJ, Yao S, Xi W, Shu M, Si R, Zhang M, Zhu JF, An CH (2019) Carbon dots decorated ultrathin CdS nanosheets enabling in-situ anchored Pt single atoms: a highly efficient solar-driven photocatalyst for hydrogen evolution. Appl Catal B-Environ 259:118036

Qu D, Zheng M, Du P, Zhou Y, Zhang LG, Li D, Tan HQ, Zhao Z, Xie ZG, Sun ZC (2013) Highly luminescent S, N co-doped graphene quantum dots with broad visible absorption bands for visible light photocatalysts. Nanoscale 5(24):12272–12277

Ri CN, Kim SG, Ju KS, Ryo HS, Mun CH, Kim UH (2018) The synthesis of a Bi_2MoO_6 /$Bi_4V_2O_{11}$ heterojunction photocatalyst with enhanced visible-light-driven photocatalytic activity. RSC Adv 8:5433–5440

Ruby S, Rosaline DR, Inbanathan SSR, Anand K, Kavitha G, Aeinivasan R (2020) Sunlight-driven photocatalytic

degradation of methyl orange based on bismuth ferrite ($BiFeO_3$) heterostructures composed of interconnected nanosheets. J Nanosci Nanotechnol 20(3):1851–1858

Shen LM, Bao NZ, Prevelige PE, Gupta A (2010) Escherichia coli bacteria-templated synthesis of nanoporous cadmium sulfide hollow microrods for efficient photocatalytic hydrogen production. J Phys Chen C114(6):2551–2559

Sun H, Liu ZG, Wang Y, Quan X, Zhao GZ (2019a) Novel metal-organic framework supported manganese oxides for the selective catalytic reduction of NO_x with NH_3: promotional role of the support. J Hazard Mater 380

Sun GT, Mao SM, Ma DD, Zou YJ, Lv YX, Li ZH, He C, Cheng YH, Shi JW (2019b) Yonghong Cheng, Jian-Wen Shi, One-step vulcanization of Cd(OH)Cl nanorods to synthesize CdS/ZnS/PdS nanotubes for highly efficient photocatalytic hydrogen evolution. J Mater Chen A 7(25):15278–15287

Wang JC, Ren J, Yao HC, Zhang L, Wang JS, Zang SQ, Han LF, Li ZJ (2016) Synergistic photocatalysis of Cr(VI) reduction and 4-Chlorophenol degradation over hydroxylated α-Fe_2O_3 under visible light irradiation. J Hazard Mater 311:11–19

Wang L, Xu X, Cheng QF, Dou SX, Du Y (2019) Near-infrared-driven photocatalysts: design, construction, and applications. Small 1904107

Yang LX, Liu M, Liu Y, Luo SL, Luo Y, Luo XB, Li GF, Peng P (2016) Theoretical analyses of organic acids assisted surface-catalyzed reduction of Cr-VI on TiO_2 nanowire arrays. Appl Catal B-Environ 198:508–515

Yi XH, Ma SQ, Du XD, Zhao C, Fu HF, Wang P, Wang CC (2019) The facile fabrication of 2D/3D Z-scheme g-C_3N_4/UiO-66 heterojunction with enhanced photocatalytic Cr(VI) reduction performance under white light. Chem Eng J 375: 121944

Yu J, Yu Y, Zhou P, Xiao W, Cheng B (2014) Morphology-dependent photocatalytic H_2-production activity of CdS. Appl Catal B-Environ 156:184–191

Yu CL, Chen FY, Zeng DB, Xie Y, Zhou WQ, Liu Z, Wei LF, Yang K, Li DH (2019) A facile phase transformation strategy for fabrication of novel Z-scheme ternary heterojunctions with efficient photocatalytic properties. Nanoscale 11(16): 7720–7733

Yu CL, Zeng DB, Fan QZ, Yang K, Zeng JL, Wei LF, Yi JH, Ji HB (2020) The distinct role of boron doping in Sn_3O_4 microspheres for synergistic removal of phenols and Cr(vi) in simulated wastewater. Environ Sci-Nano 7(1):286–303

Zeng DB, Yu CL, Fan QZ, Zeng JL, Wei LF, Li ZS, Yang K, Ji HB (2019) Theoretical and experimental research of novel fluorine doped hierarchical Sn_3O_4 microspheres with excellent photocatalytic performance for removal of Cr(VI) and organic pollutants. Chem Eng J 391:123607

Zhang GP, Chen DY, Li NJ, Xu QF, Li H, He JH, Lu JM (2019) Fabrication of Bi_2MoO_6/ZnO hierarchical heterostructures with enhanced visible-light photocatalytic activity. Appl Catal B-Environ 250:313–324

Zhu C, Liu CG, Zhou YJ, Guo SJ, Li H, Zhao SQ, Huang H, Liu Y, Kang ZH (2017) Carbon dots enhance the stability of CdS for visible-light-driven overall water splitting. Appl Catal B-Environ 216:114–121

Zhu LY, Li H, Xia PF, Liu ZR, Xiong DH (2018) Hierarchical ZnO decorated with CeO_2 nanoparticles as the direct Z-scheme heterojunction for enhanced photocatalytic activity. ACS Appl Mater Inter 10:39679–39687